Simulations of laminar flow past a superhydrophobic sphere with drag reduction and separation delay

Brian R. K. Gruncell, Neil D. Sandham, and Glen McHale

Additional information on Phys. Fluids

Simulations of laminar flow past a superhydrophobic sphere with drag reduction and separation delay

Brian R. K. Gruncell,[1,a)] Neil D. Sandham,[1] and Glen McHale[2]
[1]*Faculty of Engineering and the Environment, University of Southampton, Southampton SO17 1BJ, United Kingdom*
[2]*Faculty of Engineering and Environment, Northumbria University, Newcastle upon Tyne NE1 8ST, United Kingdom*

Superhydrophobic surfaces have potential for reducing hydrodynamic drag by combining a structured surface and hydrophobicity to retain a lubricating air layer (plastron) at the surface. In the present contribution, numerical simulations of laminar flow past a superhydrophobic sphere are conducted using a two-phase flow representation. The results show drag reductions in Stokes flow of up to 19% for an air-water system, in agreement with previous analytic work, and demonstrate an increased effect as the Reynolds number is increased to 100. Drag reductions of up to 50% are achieved due to reduction in viscous drag and suppression of separation by the plastron, resulting in a narrower wake. To explore a less idealised model of the plastron, baffles have also been introduced to simulate the support of a plastron by roughness elements. The baffles lead to the attached vortex regime no longer being suppressed, but separation is delayed and drag reductions are evident in comparison to a solid sphere. Increasing the area solid fraction results in a diminished drag reduction due to the plastron, however drag reductions of up to 15% can still be achieved with solid fractions of 10%. © *2013 AIP Publishing LLC*. [http://dx.doi.org/10.1063/1.4801450]

I. INTRODUCTION

Superhydrophobic surfaces are found frequently in nature, for example, the self cleaning Lotus leaf[1] and the ability of Fishing Spiders to retain a plastron (air layer) underwater for respiration.[2,3] In recent years, interest has arisen in mimicking superhydrophobic surfaces which can retain an air layer for the purpose of reducing hydrodynamic drag. The ability of a superhydrophobic surface to retain a plastron or air layer underwater depends on an appropriate combination of hydrophobic surface chemistry and high aspect ratio roughness.[2,4] The surface chemistry produces a high contact angle so that the surface repels water, whilst the surface roughness provides cavities such that surface tension prevents water penetration and within which air can be retained.

The presence of a plastron modifies the effective boundary condition from a no-slip condition to an air-water interface, where the velocity is non-zero and the shear stress is greatly reduced. One way of modelling this change at the wall is to use the Navier-slip model, where the surface is characterised by a slip length (λ) which depends on the slip velocity (u_s) and the velocity gradient at the wall ($\partial u/\partial n$):

$$u_s = \lambda \frac{\partial u}{\partial n}\bigg|_w. \tag{1}$$

The potential benefits of superhydrophobic surfaces have previously been explored using the Navier-slip condition over a wide range of Reynolds numbers (*Re*) from analytical models of Stokes flow[5] to direct numerical simulations of turbulent flow.[6,7] These studies demonstrate that a drag

---

a)Electronic mail: brkg105@soton.ac.uk
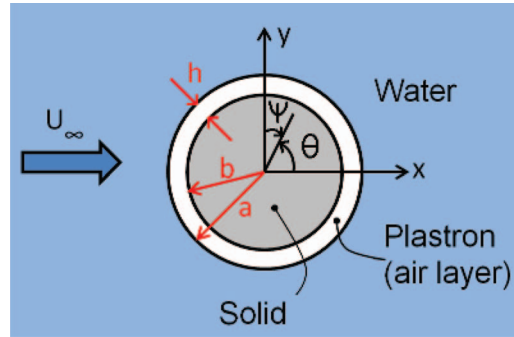
FIG. 1. Schematic of an encapsulated sphere.

reduction is possible in laminar and turbulent flow if sufficient slip can be generated at the surface. However, the Navier-slip condition only models the average effects of a superhydrophobic surface and does not simulate the interaction between the solid substrate, the air between the surface features, and the external water flow.

Improved models for superhydrophobic surfaces, including separate representations for the air and water flow, have been tested for channel flows showing a viscous drag reduction in laminar[8,9] and turbulent flow.[10] The aim of the present contribution is to apply a similar level of modelling to flow past a sphere, where additional physical flow features such as flow separation may be present. In Stokes flow, the drag coefficient (C_D) of a solid sphere can be calculated analytically[11] as

$$C_D = \frac{24}{Re}. \tag{2}$$

The drag coefficient and Reynolds number are defined classically, based on the drag of the sphere (D), free-stream velocity (U_∞), water density (ρ_w), water dynamic viscosity (μ_w), and radius of the solid sphere (b) as

$$C_D = \frac{D}{0.5\rho_w U_\infty^2 \pi b^2} \quad \text{and} \quad Re = \frac{\rho_w U_\infty 2b}{\mu_w}. \tag{3}$$

At a Reynolds number of around 0.1 the drag coefficient increases above the Stokes drag coefficient as inertial effects become important. In this range experimental correlations have been developed for the drag coefficient. The optimal fit for low Reynolds numbers is a Reynolds number modification of the Stokes drag equation,[12]

$$C_D = \frac{24}{Re}\left(1 + 0.15 Re^{0.687}\right). \tag{4}$$

McHale et al.[13] showed analytically that the Stokes drag of a solid sphere can be reduced according to a drag modification factor (ξ) if it is encapsulated in a sphere of a less viscous fluid as shown in Figure 1. The drag modification factor (ξ) is calculated based on the ratio of the drag between a solid sphere (radius b) and the same solid sphere encapsulated in a plastron (thickness h, such that the composite sphere has a larger radius $b + h$),

$$\xi = \frac{\text{(Drag of sphere with plastron)}}{\text{Drag of sphere}}. \tag{5}$$

A value of $\xi < 1$ signifies an overall reduction in drag of the encapsulated sphere. The drag modification factor depends on the relative radius of the encapsulated sphere ($\varepsilon = b/a$) and the ratio of dynamic viscosity between the two fluids ($\mu_{aw} = \mu_a/\mu_w$) and for Stokes flow can be calculated using

$$\xi = \frac{2}{3\varepsilon}\left[\frac{1 + 3\mu_{aw}F(\varepsilon)}{1 + 2\mu_{aw}F(\varepsilon)}\right], \tag{6}$$

where

$$F\left(\varepsilon\right) = \frac{\left(1+\varepsilon\right)\left(2\varepsilon^2 + \varepsilon + 2\right)}{\left(1-\varepsilon\right)\left(4\varepsilon^2 + 7\varepsilon + 4\right)}. \tag{7}$$

The encapsulated sphere is a model of perfect hydrophobicity, where the water is no longer in contact with the solid body. Such a perfect state may also be achieved using the Leidenfrost effect,[14] where the surface is heated significantly above the boiling temperature of the fluid, creating an insulating vapour layer between the surface and the fluid. The presence of an encapsulating layer on the terminal velocity of a sphere has been explored experimentally by McHale *et al.*[15] and Vakarelski *et al.*[16] at high Reynolds number ($10^4 < Re < 10^5$) showing drag reductions of up to 15% and 85%, respectively. In each case the drag mechanism is postulated to be a reduced shear at the sphere surface resulting in a delay in separation. The primary difference between the two studies is the mechanism for retaining a plastron on the surface, with the former using randomly structured superhydrophobic surfaces and the latter using the Leidenfrost effect. The random roughness supporting the plastron in the superhydrophobic case ensures that the plastron is energetically stable over time, whilst continuous heating is required to maintain the Leidenfrost plastron for more than a minute. However, the roughness contributes to a composite interface, rather than a perfectly encapsulated sphere, resulting in a lower drag reduction. A combination of the Leidenfrost effect (to generate the vapour layer) and a rough superhydrophobic surface (to retain it) has recently been suggested.[17]

Numerical simulations have been conducted on a plastron-encapsulated sphere at low Reynolds numbers, with attempts to model a composite interface with slip at the surface[18] and using a reduced viscosity through a simple application of the VOF (Volume of Fluid) model.[19] These results demonstrate the possibility of drag reduction and delay of separation at finite Reynolds numbers. However, the models are based on assuming it is possible to retain an air layer at the surface and they do not facilitate the design of superhydrophobic surfaces capable of achieving such an effect.

The present contribution aims to explore the potential for drag reduction on an encapsulated sphere, whether the plastron is sustained by hydrophobicity, or the Leidenfrost effect, or a combination of both. The plastron is directly included by modelling both the air and water phases. Simulations are conducted to explore the gap between an idealised perfect plastron in Stokes flow and a plastron which is stable over long immersion periods at higher Reynolds numbers.

II. NUMERICAL MODEL

A. Axisymmetric approach and solver

To simulate the flow past a superhydrophobic sphere the Navier-Stokes equations have been solved using a finite volume approach in two coupled domains. The simulations have been conducted to match an air-water system with fluid properties $\rho_w/\rho_a = 815.00$ and $\mu_w/\mu_a = 56.05$. For Reynolds numbers below approximately 130 the flow past a sphere is steady and axisymmetric,[20] furthermore slip at the surface delays the typical flow regimes for a sphere to a higher Reynolds number.[18, 19] It is possible that the slip/no-slip composite interface may promote a 3D instability but it is considered to be beyond the scope of this work. Hence, the simulation is simplified in the present work by assuming that the flow is axisymmetric with an axis of rotation along the *x*-axis. For convenience, the problem was solved using the commercial CFD package Fluent$^{\text{TM}}$ (Fluent, Inc., New Hampshire). The flow is entirely laminar so no turbulence model is required and the major source of inaccuracy in a CFD package is removed. The code is used to solve the Navier-Stokes equations

$$\rho\frac{\partial \boldsymbol{u}}{\partial t} + \rho\left(\boldsymbol{u}\cdot\nabla\boldsymbol{u}\right) = -\nabla P + \mu\nabla^2\boldsymbol{u}, \tag{8}$$

with

$$\nabla\cdot\boldsymbol{u} = 0. \tag{9}$$

The boundary conditions used are a no-slip condition at the solid sphere surface ($\boldsymbol{u} = 0$), constant axial velocity at the inlet ($\boldsymbol{u} = [u_i, 0, 0]$), and a pressure outlet where the gauge pressure is set to zero. The boundary condition at the air-water interface is discussed in detail in Sec. II B. The SIMPLEC pressure-correction algorithm is used to aid convergence and 2nd order spatial discretisation is used to improve accuracy. Each simulation is run in a steady state mode until convergence has been achieved. Convergence is achieved when reducing the average residual ($|R|$) within the domain by an order of magnitude does not influence the drag by more than 1%. The required residual level was checked across the range of Reynolds numbers and plastrons explored in this study and was found to be in the range of $|R| = 10^{-6}$ to $|R| = 10^{-7}$, with thinner plastrons and higher Reynolds numbers being more sensitive to the convergence level.

B. Modelling of the plastron

The plastron is initially modelled as a layer of air (with fluid properties ρ_a and μ_a) with a constant thickness ($h = a - b$). The two phases (air and water) are considered as two distinct fluids in two separate domains. The air-water interface is treated as being fixed in space and does not deform due to the applied viscous or pressure forces. The coupling between the two phases is conducted through the boundary condition at the air-water interface. To ensure the correct physical behaviour at the interface three conditions have to be imposed. First, the tangential velocity components at the interface have to be matched. Second, the shear stress components tangential to the interface also have to match. Finally, there has to be zero mass transfer across the interface. To impose these three conditions a new boundary condition has been developed through the use of User-Defined Functions (UDF) and User-Defined Memory (UDM). The approach involves a two-way coupling where information from the air domain is used to impose a boundary condition in the water domain and vice-versa; the method is discussed further in the Appendix. This is an idealised model of the air-water interface in that it is assumed that the interface will not deform. This assumption is valid when the contact line is pinned at the top of the roughness elements (which is likely due to a local energy barrier at the discontinuity in curvature[21]) and the Capillary number (ratio of viscous to surface tension effects) is low. It is inherent in this assumption that the Cassie-Baxter state is maintained and that the surface tension and roughness prevents capillary penetration causing the wetting out of the cavities (i.e., a transition to the Wenzel state). The interface is assumed to match the curvature of the solid sphere such that the composite interface is itself spherical in shape. Vakarelski et al.[16] demonstrated that at a Reynolds number in the range $10^4 - 10^5$ the Leidenfrost effect can be used to produce a nearly completely smooth spherical encapsulating air layer. It is postulated that, at the significantly lower Reynolds numbers explored in this study, an idealised spherical shape is an accurate approximation. However, the results presented in this report should be considered as an optimal case; any interface deformation will likely result in decreased performance of the plastron.

C. Mesh generation

To ensure that the solution is fully resolved mesh dependency studies have been conducted. First, considering Stokes flow, it was found that the drag only matched the analytic theory[11] of a sphere in freestream when the far-field was at $500b$. This is in contrast to the higher Reynolds number range where the domain size could be set to $50b$ and achieve domain size independent results. Furthermore, the regions requiring high grid resolution differ between Stokes flow and higher Reynolds numbers, with the former only requiring high resolution close to the sphere and the latter also requiring high resolution in the wake. A sketch of the domains used for the low ($Re < 1$) and high ($1 < Re < 100$) Reynolds number cases are shown in Figure 2.

A structured Cartesian grid has been used for the low Reynolds number mesh, with a semi-circular domain. For the high Reynolds number mesh a multi-block approach with an unstructured mesh has been used, allowing a higher resolution close to the sphere and in the wake, whilst maintaining a low resolution in the far-field and ensuring a high mesh quality. Initial studies were conducted to explore the overall mesh resolution, with the mesh resolution being successively doubled until a grid independent solution (to within 1%) was obtained for a solid sphere across the
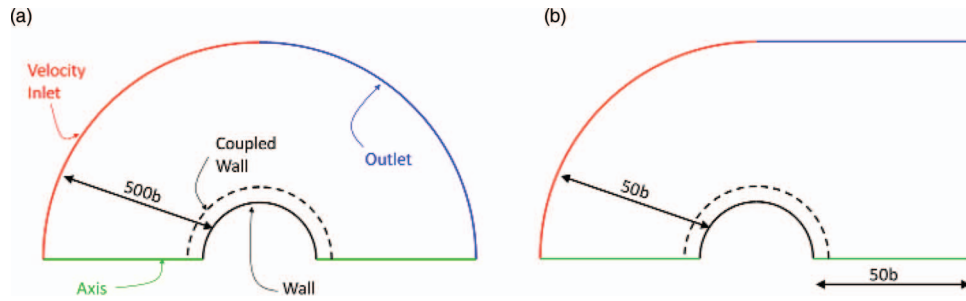
FIG. 2. Schematic of domain shape and size used for (a) low Reynolds number range and (b) high Reynolds number range (not to scale).

full Reynolds number range explored. A typical mesh for the data presented included approximately 1200 grid points along the semi-circular edge of the sphere and 40 grid points across the plastron. Figure 3 demonstrates the successive doubling of mesh resolution and convergence of the results towards a grid independent solution (the percentage change in drag shown is based on the finest grid in each case). The solution converged to the empirical relation (Eq. (4)) for a solid sphere, matching to better than 1% across entire Reynolds number range explored.

As the Reynolds number increases the solution becomes more dependent on the mesh used, as shown in Figure 3. For simulations with a plastron the mesh resolution was held approximately constant for radial positions further than $2b$ from the sphere surface, whilst an unstructured quadrilateral mesh was applied in the region close to the plastron. The mesh within and close to the plastron was again successively refined until the drag and velocity profiles within the wake and plastron were grid independent. For simulations with baffles (see Sec. IV B) the grid was further refined so that the grid points were highly focused around the tips of the baffles. Doubling the resolution demonstrated mesh independence in both the viscous and pressure drag components.

III. VALIDATION AND VERIFICATION

A range of studies has been conducted to ensure that the approach described in Sec. II is capable of capturing first the drag on a solid sphere and second the drag of a solid sphere encapsulated in a plastron. First, the flow past a solid sphere has been simulated over the Reynolds number range $0.0001 < Re < 100$. The low Reynolds number meshes were used up to $Re = 1$, whilst the high Reynolds number meshes were used above $Re = 1$. The two meshes produced the same drag to within 1% at $Re = 1$. Grid convergence and residual independence allows each of the drag values to be cited to an accuracy within $\pm 1\%$ unless otherwise stated. Figure 4 demonstrates that the simulations accurately capture the drag coefficient of a solid sphere over a wide Reynolds number
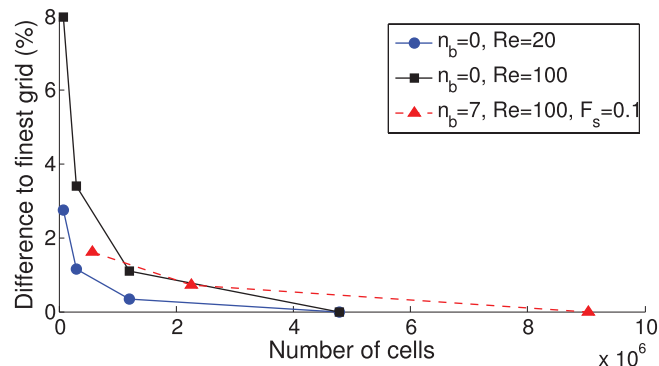
FIG. 3. Grid refinement study for a solid and plastron-encapsulated spheres.
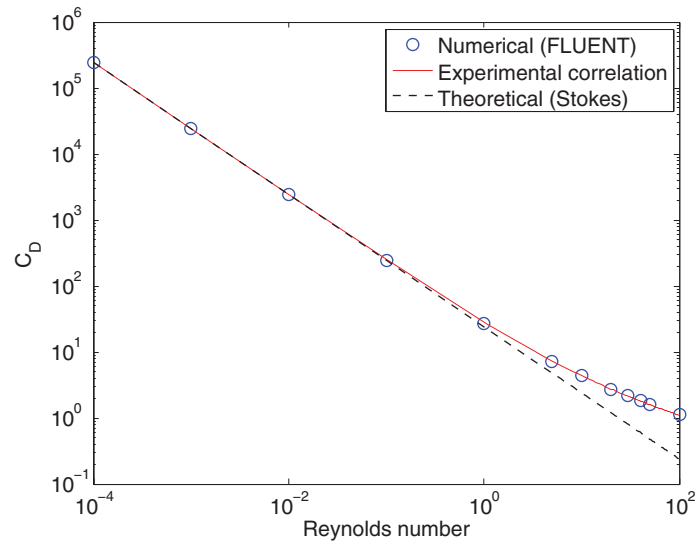
FIG. 4. Drag coefficient of solid sphere across a wide Reynolds number range.

range, including the departure from Stokes theory at high Reynolds number. A separation angle, θ_s (using the convention for θ in Figure 1), is defined using the change in sign in the tangential velocity at the first cell centre off the wall. It was verified, as shown in Figure 5 that the simulations accurately match the onset of separation at $Re \approx 24$ and the variation of separation angle with Reynolds number.[20]

Second, simulations have been conducted to explore whether the coupled interface model can be used to simulate superhydrophobic spheres. A range of plastron thicknesses have been explored in Stokes flow to allow a comparison to the analytic theory.[13] Figure 6 shows that the theoretical drag reduction due to the presence of the plastron around the sphere is matched well by the coupled interface simulations. Furthermore, Figure 7 shows that the velocity profiles in both the air layer and external water flow field match theoretical results deduced from the streamfunctions given in McHale *et al.*[13] The velocity profile demonstrates the generation of slip at the air-water interface ($\sim 0.4 U_\infty$) and the discontinuous velocity gradient due to the matched shear stress but difference
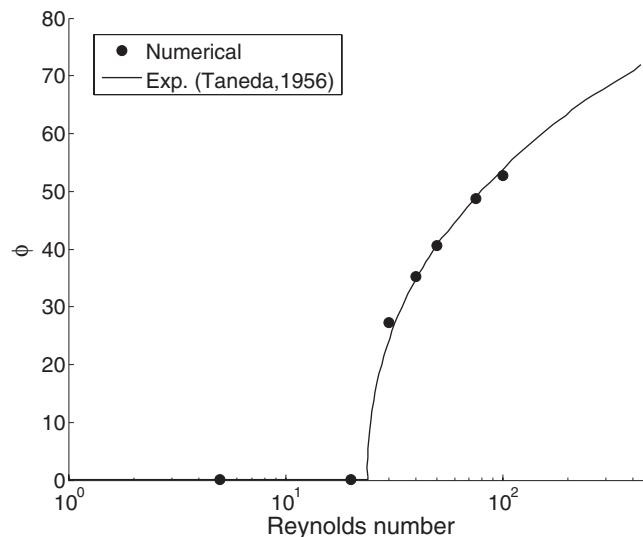
FIG. 5. Dependence of separation angle on Reynolds number for a solid sphere.
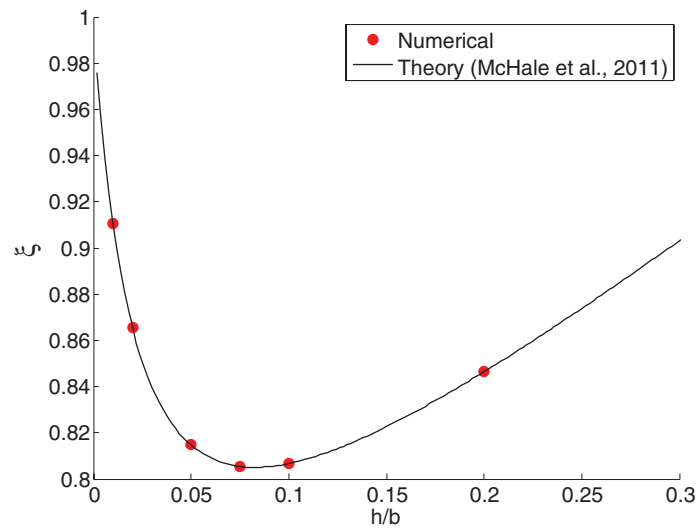
FIG. 6. Drag reduction due to plastron in Stokes flow.

in dynamic viscosities of the two fluids. This suggests that the coupled interface model accurately captures the physics associated with the presence of a plastron.

IV. RESULTS

A. Idealised model

For Stokes flow, in agreement with the analytic theory, a maximum drag reduction of 19% is obtained from Figure 6. The drag reduction depends on the thickness of the air layer, with the optimal air layer thickness being approximately $0.1b$. Below this optimum value, the drag reduction decreases with decreasing air layer thickness; the thicker air layer supports a larger circulation and produces less viscous drag at the interface. Above this value, the thickness of the plastron increases the effective frontal area of the sphere and the increase in pressure drag begins to dominate over the reduction in viscous drag.
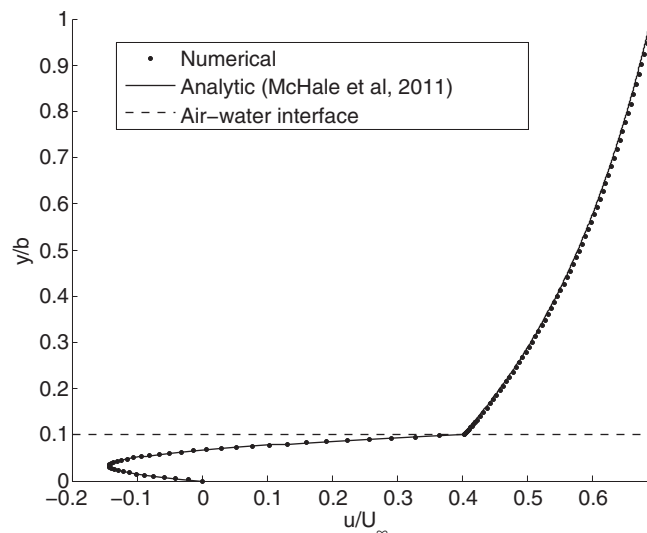
FIG. 7. Axial velocity at the top of the sphere ($Re = 0.001$, $h/b = 0.1$).
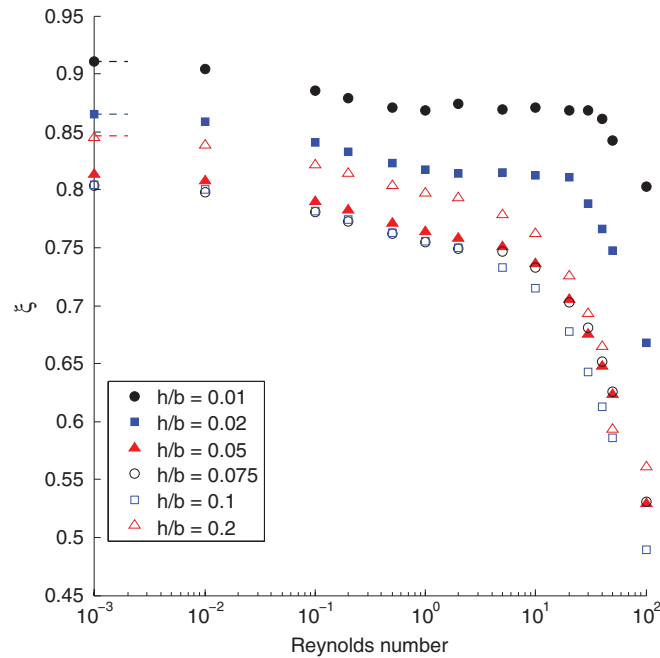
FIG. 8. Effect of the plastron on drag reduction factor (ξ) for a range of plastron thicknesses.

Figure 8 shows the effect of increasing the Reynolds number of the external flow. The value of ξ slowly decreases as the Reynolds number increases from $Re = 0.01$. As the Reynolds number is increased above 10 a larger drag reduction is evident, up to 50% for $h/b = 0.1$ at $Re = 100$. This increased drag reduction was found to be associated with the suppression of the attached vortex regime in the Reynolds number range $30 < Re < 100$ as demonstrated in Figure 9. The reduced shear stress and finite slip velocity at the air-water interface mean that separation from the downstream surface of the sphere is completely suppressed, resulting in a narrower wake. The optimal plastron thickness remains approximately constant throughout the Reynolds number range explored, with the estimated error in the results being close to the size of the symbols in Figure 8. It is important to note that a drag reduction of around 10% is achieved for the thinnest plastron tested ($0.01b$) and that the vortex is still suppressed in this case. This suggests that a large drag reduction can be achieved with a small modification to a surface coating.

The results described in this section are for a solid sphere which is encapsulated in a sphere of air. This is an idealised (perfectly hydrophobic) case where the water does not touch the solid surface. For a superhydrophobic surface, the percentage of the surface covered in solid, or solid fraction (F_S), could not be exactly 0%, as the plastron needs to be supported by roughness elements. Furthermore, it has been assumed that the air-water interface is fixed in position, which is unlikely unless there is some structure beneath the plastron, to which the contact line could be pinned. This structure within the plastron would act to split the single circulation cell that is evident in Figure 9(b). To explore these issues and the effect of solid fraction on the drag reduction a series of baffles are introduced.

B. Baffles

In most previous studies, the Navier-slip condition[6,22] or alternating regions of no-slip and full-slip[5,23] have been used to model the effect of the hydrophobic surface. The first approach provides an averaged effect of the hydrophobicity, assuming a homogeneous surface. In the second approach, the effect of solid fraction is explored by making the solid area smaller until F_S approaches zero. In Sec. IV A an idealised hydrophobic sphere provides a theoretical maximum
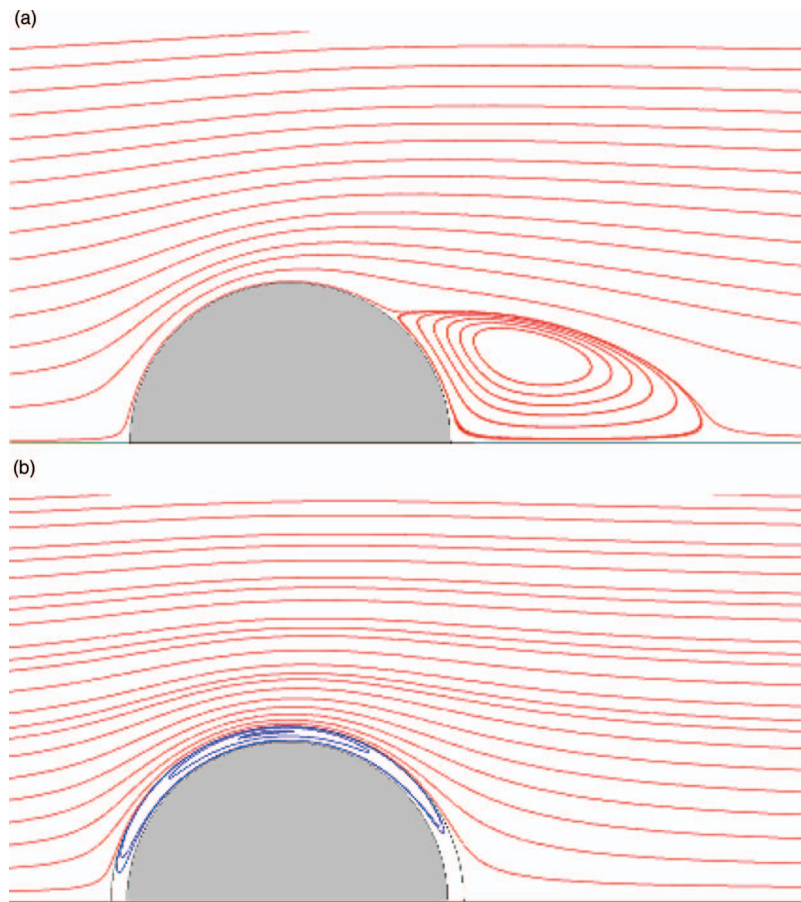
FIG. 9. Streamlines past (a) a solid sphere and (b) plastron-encapsulated sphere ($h/b = 0.1$) at $Re = 100$ showing separation suppression.

drag reduction. With the introduction of baffles we now aim to explore the departure away from this idealised case, whilst maintaining a more realistic model of an inhomogeneous hydrophobic surface. The baffles introduced in this study are ribs that extend from the solid sphere to the air-water interface (Figure 10). They are aligned perpendicular to the freestream and are axisymmetric about an axis parallel to the freestream as shown in Figure 11. The baffles can be characterised by two parameters: the number of baffles (n_b) and the area solid fraction of the total sphere surface ($F_S = A_{\text{interface}}/A_{\text{total}}$). The baffles are placed such that they are equally spaced and the angle subtended by each baffle is constant. In the special case of $F_S = 0$ and $n_b \neq 0$ the baffles are present but have zero thickness; these baffles are treated as double-sided walls with the no-slip condition applied on either side and zero mass or momentum transfer across the wall.
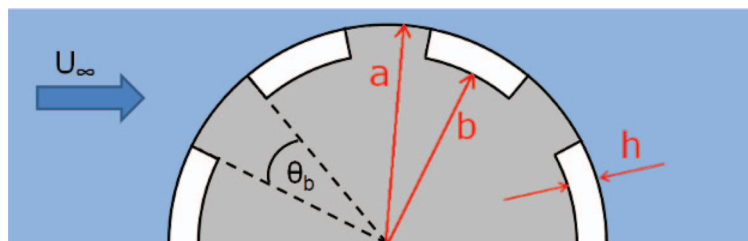
FIG. 10. Schematic of baffle configuration.
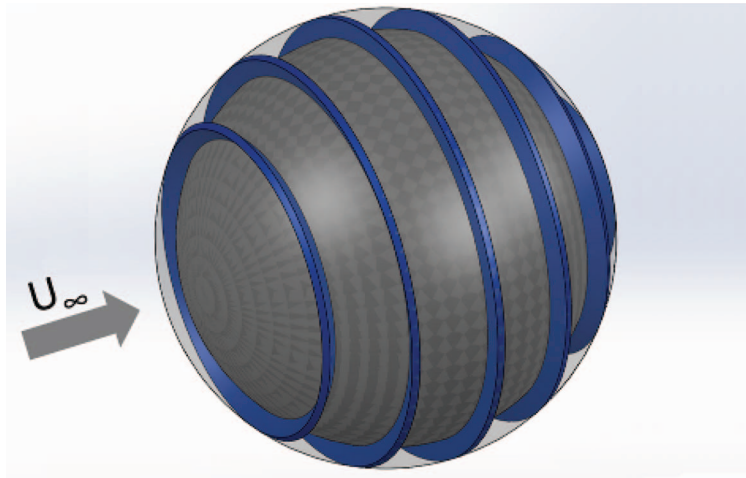
FIG. 11. Model of solid sphere with axisymmetric baffles and plastron.

The effect of infinitely thin baffles on the circulation within the plastron is demonstrated in Figure 12. The presence of 7 baffles breaks the original single circulation cell into 8 smaller circulation cells. The zero thickness of the baffles means that the external fluid flows over only the air-water interface; there is still no contact between the external fluid and the sphere. However, the drag reduction effect is abated due to reduced interfacial velocity around the edges of the baffles as shown in Figure 13.

The deficit in interfacial velocity at the edges of the baffles results in a reduction in the local slip and hence an increase in the local shear stress (Figure 14). Clearly, increasing the number
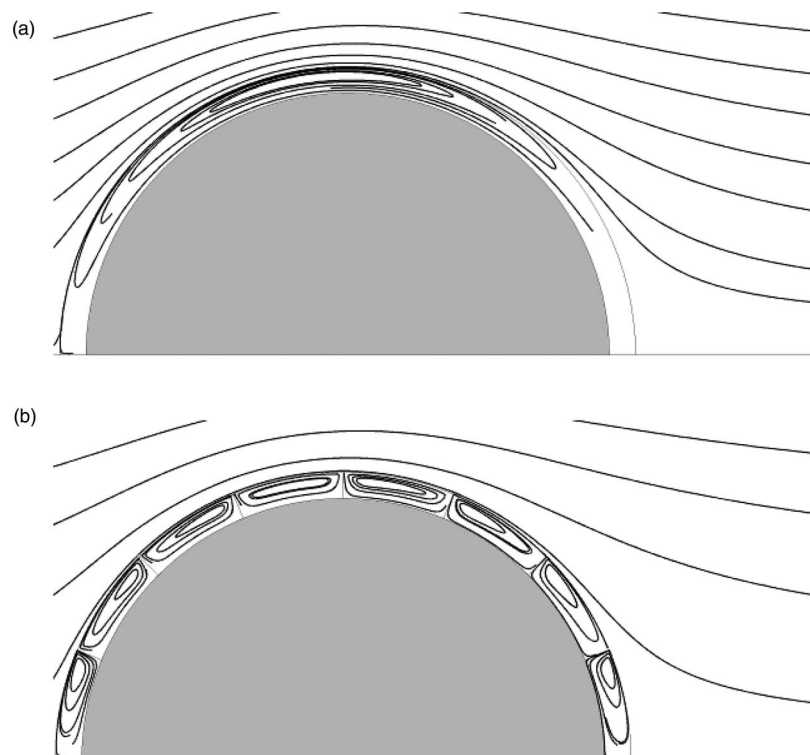
FIG. 12. Pathlines past an encapsulated sphere (a) without baffles and (b) with baffles ($Re = 100$).
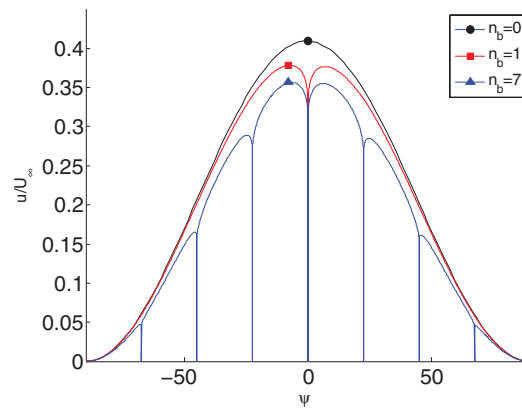
FIG. 13. Interfacial axial velocity component with zero thickness baffles ($Re = 0.1$, $h/b = 0.1$).

of baffles increases the percentage of the surface area where the interfacial velocity is lower than the idealised case and therefore decreases the effect of the plastron. The overall impact of increasing the number of baffles is to decrease slightly the drag reduction as shown in Figure 15. However, the attached vortex regime remains suppressed with the presence of zero thickness baffles.

The error bars shown in Figure 15 demonstrate that it is difficult to achieve grid independence with zero thickness baffles for a large number of baffles, especially at high Reynolds numbers. This is because of the singular point at the tip of each baffle. To overcome this issue and explore a more realistic situation, the effect of finite baffle thickness has been explored. The baffles are each assumed to subtend the same angle (θ_b), which is calculated for each case to achieve a certain area solid fraction (F_S) of the total surface area of the sphere. This means that the external flow will experience patches of no-slip (at the solid baffles) and partial slip (at the air-water interface).

The presence of finite-thickness baffles results in the attached vortex regime no longer being suppressed in the majority of cases and hence the decrease in drag is lower as shown in Figure 16. In fact at higher Reynolds numbers and high cavity fractions the drag reduction disappears completely and the presence of the plastron, combined with the baffles, produces an overall drag increase.
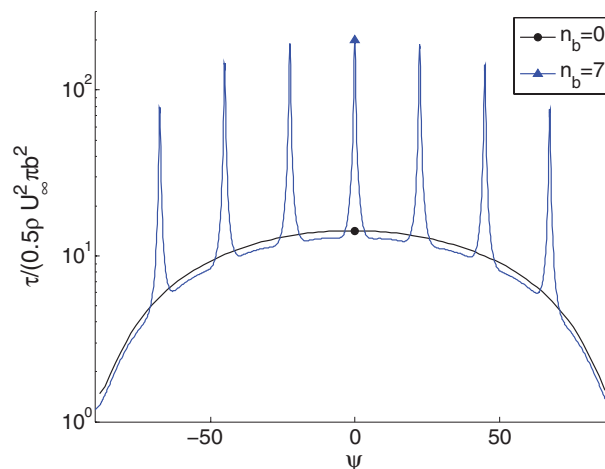
FIG. 14. Interfacial shear stress profiles with zero thickness baffles ($Re = 0.1$, $h/b = 0.1$).
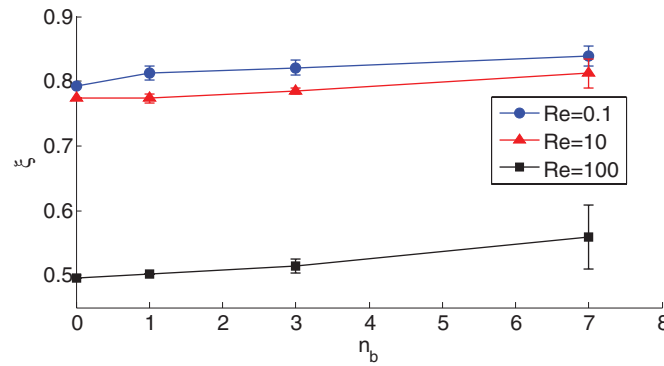
FIG. 15. Effect of addition of zero thickness baffles on drag reduction ($h/b = 0.1$).

There are three related effects which contribute to the overall drag. First, the slip at the air-water interface acts to reduce the shear stress and hence the viscous drag. Second, the combination of no-slip and slip patches affects the separation location, which in turn affects the pressure drag. Third, increasing F_S results in an increase in the relative blockage of the sphere. The increase in blockage becomes the dominant parameter as F_S tends to 1 where the plastron acts to produce an overall drag increase, approaching the drag of a solid sphere of radius $(b + h)$.

Figure 17 demonstrates that the drag reduction collapses with the separation angle, suggesting that separation is the key physical process controlling the drag. The increase in the relative blockage ratio and associated pressure drag is important because for the same separation angle as for the original solid sphere of radius b there is an increase in drag. The overall breakdown of the pressure (C_{DP}), viscous (C_{DV}), and total (C_{DT}) drag coefficients is given in Table I along with the change in drag coefficients ($\%C_{DP}$, $\%C_{DV}$, and $\%C_{DT}$, respectively, where $\%C_{DT} = 100(\xi - 1)$) in comparison to a solid sphere. It is clear that the overall effect of the plastron is to increase the pressure drag but decrease the viscous drag. The increase in pressure drag can be attributed to an increase in the overall frontal area, whilst the decrease in viscous drag is due to the reduced shear at the air-water interface. The viscous drag is the main contributor and results in an overall drag reduction. At higher Reynolds numbers the delay in separation results in a narrower wake and smaller increase in pressure drag.
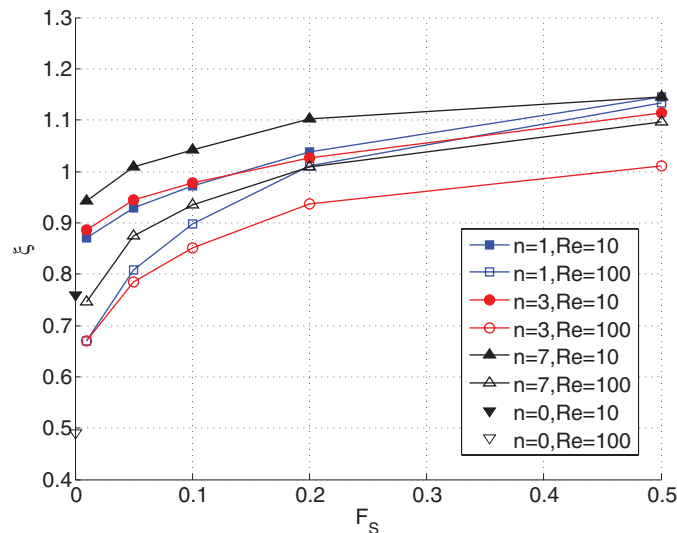
FIG. 16. Drag reduction for different baffle configurations at $Re = 10$ and $Re = 100$ ($h/b = 0.1$).
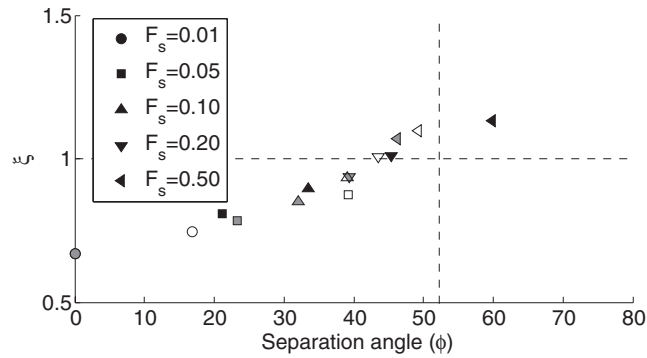
FIG. 17. Relation between separation angle and overall drag value ($Re = 100$, $h/b = 0.1$). White symbols: $n_b = 1$, grey: $n_b = 3$, black: $n_b = 7$. The dashed line is for a no-slip sphere.[20]

The primary influence of the baffles, whether through increasing n_b or F_s, is a diminished viscous drag reduction. This is due to an increase in the total surface area subject to the no-slip condition and a decrease in the length of the fetch for each cavity, resulting in a lower induced velocity within the cavity. Figure 17 also demonstrates that although the drag is primarily affected by the separation angle the solid fraction is also important. For example, for $n_b = 1$ and $F_s = 0.05/0.1$ the same separation angle produces a different drag value.

In the case with finite thickness baffles, the magnitude of the recirculation velocities within each cavity and the associated interfacial velocities are significantly reduced, as shown in Figure 18. The velocity is forced to zero at the tops of the baffles due to the no-slip condition, resulting in a new boundary layer forming and hence a lower interfacial velocity. The shear stress on the baffles is approximately two orders of magnitude higher than at the air-water interface, resulting in a reduced effect (Figure 19). This lower interfacial velocity and increased shear stress will clearly influence the location of the separation point.

Finally, it is interesting to note that the separation point does not move in discrete steps from the edge of each of the baffles. Instead, the separation location moves continuously along the rear of the sphere. In some cases the separation location is mid-way along a section of air-water interface, creating two separate and opposite recirculation cells within a cavity. In this case, the air-water interface is actually acting to promote separation slightly, due to the upstream component of velocity at the air-water interface as a result of slip within the recirculation region as shown in Figure 20.

TABLE I. Comparison between the pressure and viscous drag contributions for a solid sphere and a plastron-encapsulated sphere with baffles (C_{DP} = pressure drag coefficient, C_{DV} = viscous drag coefficient, C_{DT} = total drag coefficient).

Re	n_b	F_s	C_{DP}	C_{DV}	C_{DT}	$\%C_{DP}$	$\%C_{DV}$	$\%C_{DT}$
10	. . .	. . .	1.53	2.81	4.34	. . .	. . .	. . .
10	1	0.01	3.13	0.48	3.62	+105.1	−82.8	−16.6
10	1	0.20	2.59	1.72	4.31	+69.5	−38.9	−0.7
10	7	0.01	2.90	1.01	3.91	+90.0	−64.1	−9.9
10	7	0.20	2.22	2.28	4.51	+45.6	−18.8	+3.8
100	. . .	. . .	0.52	0.59	1.12	. . .	. . .	. . .
100	1	0.01	0.61	0.13	0.74	+17.4	−78.5	−33.5
100	1	0.20	0.72	0.39	1.12	+38.2	−33.6	+0.1
100	7	0.01	0.63	0.20	0.82	+19.5	−66.6	−26.2
100	7	0.20	0.64	0.47	1.11	+22.7	−20.1	−0.1
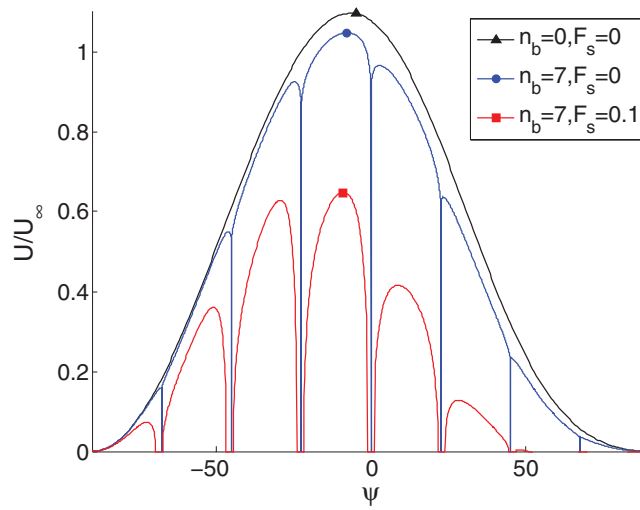
FIG. 18. Interfacial velocity profiles for a range of baffle configurations ($Re = 100$, $h/b = 0.1$).
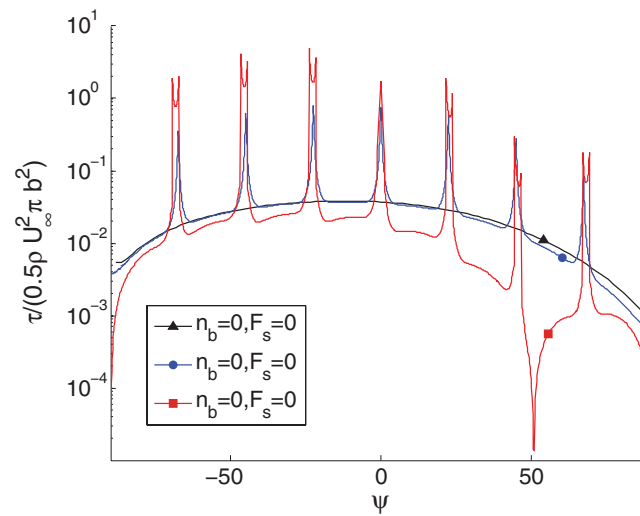
FIG. 19. Interfacial shear profiles for a range of baffle configurations ($Re = 100$, $h/b = 0.1$).
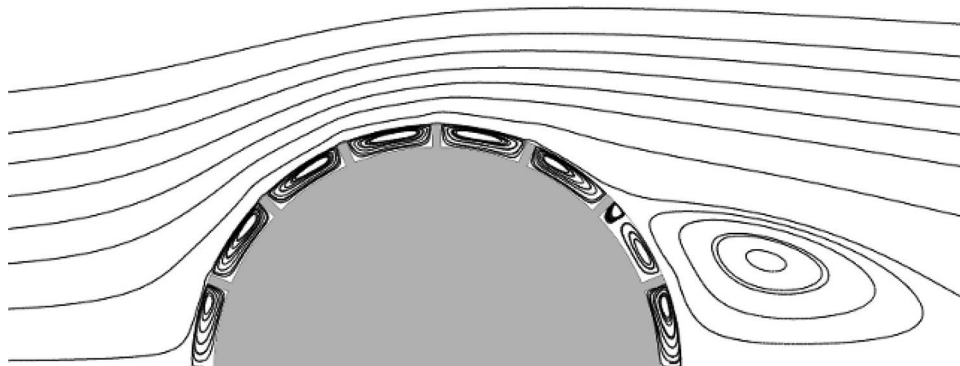
FIG. 20. Pathlines showing separation from the middle of a cavity section ($F_S = 0.1$, $Re = 100$, $h/b = 0.1$).

V. CONCLUSIONS

Numerical simulations of a sphere encapsulated in a plastron, or a layer of air, from Stokes flow up to a laminar Reynolds number of 100 have been reported. The presence of the plastron produces a drag reduction that matches the analytic solution in Stokes flow and increases to a maximum of 50% at the higher Reynolds numbers. A finite slip velocity and reduced shear stress at the air-water interface result in the complete suppression of the usual attached vortex regime, where the flow is separated but still steady, typically for spheres seen in the range $24 < Re < 130$.

Baffles are included in the simulations to match a realistic situation where the plastron is supported by roughness elements, producing a composite interface. The baffles produce a degradation of the drag reduction as they reduce the circulation within each section of the plastron. As the solid fraction increases, separation is no longer completely suppressed, although it is delayed and a drag reduction is still possible. However, if the solid fraction is increased above approximately 10% then the presence of a plastron produces an overall drag increase even though separation is delayed.

Overall it is clear that a surface retaining a plastron composed of a complete air layer, or one which is a composite of several cells, can produce a reduction in the viscous drag. Furthermore, the presence of a plastron can reduce the local shear and hence completely suppress or delay separation. However, it is salient that it is the detailed surface geometry rather than an averaged effect that is important in determining the overall potential for drag reduction.

ACKNOWLEDGMENTS

APPENDIX: APPLICATION OF THE COUPLED INTERFACE BOUNDARY CONDITION

A coupled boundary condition is used to represent the air-water interface. The main issues with this approach are the transfer of data across the interface and ensuring that the data from one side of the interface is transferred to the correct location on the opposite side. The matching of the tangential velocity across the interface is relatively simple as it only involves the transfer of the two components of velocity across the interface. However, the matching of the tangential shear stress is more convoluted, as it requires a conversion from Cartesian coordinates to surface normal coordinates and then back to Cartesian. In tensor notation the shear stress can be expressed as

$$\tau_{ij} = \mu \left(\frac{\partial u_i}{\partial x_j} + \frac{\partial u_j}{\partial x_i} \right). \tag{A1}$$

For a curved surface the Cartesian coordinate system is replaced with a coordinate system aligned with the surface. At each point the Cartesian system can be rotated by an angle (θ) so that the x-axis becomes aligned with the surface (s-axis) and the y-axis becomes the surface normal direction (n-axis). To calculate τ_{sn} requires velocity gradients in the surface normal coordinate system and these can be calculated based on the gradients in the Cartesian system using a tensor rotation matrix

$$\nabla \mathbf{u}' = \mathbf{A} \nabla \mathbf{u} \mathbf{A}^T, \tag{A2}$$

where

$$\nabla \mathbf{u} = \begin{pmatrix} \frac{\partial u}{\partial x} & \frac{\partial v}{\partial x} \\ \frac{\partial u}{\partial y} & \frac{\partial v}{\partial y} \end{pmatrix} \quad \text{and} \quad \mathbf{A} = \begin{pmatrix} \cos\theta & -\sin\theta \\ \sin\theta & \cos\theta \end{pmatrix}. \tag{A3}$$

The values of $\cos\theta$ and $\sin\theta$ can be calculated easily if the sphere has its centre located at the origin by using the position of the centre of each face on the boundary (**P**):

$$\cos\theta = \frac{P_x}{|\mathbf{P}|} \qquad \sin\theta = \frac{P_y}{|\mathbf{P}|}. \tag{A4}$$

The boundary conditions are applied in a Cartesian coordinate system and hence the final value of wall shear stress needs to be projected in the x- and y-directions

$$\tau_x = \tau_{sn}\cos\theta \qquad \tau_y = \tau_{sn}\sin\theta. \tag{A5}$$

The values for tangential shear stress and tangential velocity are calculated at the start of each iteration based on the values from the previous iteration and then applied as a boundary condition.

[1] W. Barthlott and C. Neinhuis, "Purity of the sacred lotus, or escape from contamination in biological surfaces," Planta **202**, 1–8 (1997).

[2] N. J. Shirtcliffe, G. McHale, M. I. Newton, C. Perry, and F. Pyatt, "Plastron properties of a super-hydrophobic surface," Appl. Phys. Lett. **89**, 104106 (2006).

[3] M. R. Flynn and J. W. Bush, "Underwater breathing, the mechanics of plastron respiration," J. Fluid Mech. **608**, 275–296 (2008).

[4] J. P. Rothstein, "Slip on superhydrophobic surfaces," Annu. Rev. Fluid Mech. **42**, 89–109 (2010).

[5] J. R. Phillip, "Flows satisfying mixed no-slip and no-shear conditions," Z. Angew. Math. Phys. **23**, 353–370 (1972).

[6] T. Min and J. Kim, "Effects of hydrophobic surface on skin friction drag," Phys. Fluids **16**, L55–L58 (2004).

[7] A. Busse and N. D. Sandham, "Influence of an anisotropic slip-length boundary condition on turbulent channel flow," Phys. Fluids **24**, 055111 (2012).

[8] P. Gao and J. J. Feng, "Enhanced slip on a patterned substrate due to depinning of contact line," Phys. Fluids **21**, 102102 (2009).

[9] J. Davies, D. Maynes, B. W. Webb, and B. Woolford, "Laminar flow in a microchannel with superhydrophobic walls exhibiting transverse ribs," Phys. Fluids **18**, 087110 (2006).

[10] K. Jeffs, D. Maynes, and B. W. Webb, "Prediction of turbulent channel flow with superhydrophobic walls consisting of micro-ribs and cavities oriented parallel to the flow direction," Int. J. Heat Mass Transfer **53**, 786–796 (2010).

[11] J. Happel and H. Brenner, *Mechanics of Fluids and Transport Processes* (Martinus Nijhoff Publishers, Leiden, 1986).

[12] R. Clift, J. R. Grace, and W. E. Weber, *Bubbles, Drops and Particles* (Academic Press, New York, 1978).

[13] G. McHale, M. R. Flynn, and M. I. Newton, "Plastron induced drag reduction and increased slip on a superhydrophobic sphere," Soft Matter **7**, 10100–10107 (2011).

[14] J. G. Leidenfrost, "De aquae communis nonnullis qualitatibus tractatus," (1756), transl. C. Wares, "On the fixation of water in diverse fire," Int. J. Heat Mass Transfer **9**, 1153–1166 (1966).

[15] G. McHale, N. J. Shirtcliffe, C. R. Evans, and M. I. Newton, "Terminal velocity and drag reduction measurements on superhydrophobic spheres," Appl. Phys. Lett. **94**, 064104 (2009).

[16] I. Vakarelski, J. Martson, D. Chan, and S. Thoroddsen, "Drag reduction by Leidenfrost vapour layers," Phys. Rev. Lett. **106**, 214501 (2011).

[17] I. Vakarelski, N. Patankar, J. Martson, D. Chan, and S. Thoroddsen, "Stabilization of Leidenfrost vapour layer by textured superhydrophobic surfaces," Nature (London) **489**, 274–277 (2012).

[18] G. Atefi, H. Niazmand, and M. R. Meigounpoory, "Numerical analysis of 3-D flow past a stationary sphere with slip condition at low and moderate Reynolds numbers," J. Dispersion Sci. Technol. **28**, 591 (2007).

[19] Z.-G. Feng, "A correlation of the drag force coefficient on a sphere with interface slip at low and intermediate Reynolds numbers," J. Dispersion Sci. Technol. **31**, 968–974 (2010).

[20] S. Taneda, "Experimental investigation of the wake behind a sphere at low Reynolds numbers," J. Phys. Soc. Jpn. **11**, 1104–1108 (1956).

[21] B. He, N. A. Patankar, and J. Lee, "Multiple equilibrium droplet shapes and design criterion for rough hydrophobic surfaces," Langmuir **19**, 4999–5003 (2003).

[22] A. Niavarani and N. V. Priezjev, "The effective slip length and vortex formation in laminar flow over a rough surface," Phys. Fluids **21**, 052105 (2009).

[23] Y. Cheng, C. J. Teo, and B. C. Khoo, "Microchannel flows with superhydrophobic surfaces, effects of Reynolds number and pattern width to channel height ratio," Phys. Fluids **21**, 122004 (2009).